Reflected light microspectroscopy for single-nanoparticle biosensing

Sergiy Patskovsky
Michel Meunier

Reflected light microspectroscopy for single-nanoparticle biosensing

Sergiy Patskovsky* and Michel Meunier
École Polytechnique de Montréal, Engineering Physics Department, Laser Processing and Plasmonics Laboratory,
Montréal, Québec, H3C 3A7, Canada

Abstract. Conventional and dark-field microscopy in the transmission mode is extensively used for single plasmonic nanoparticle (NP) imaging and spectral analysis. However, application of the transmission mode for real-time biosensing to single NP poses strict limitations on the size and material properties of the microfluidic system. This article proposes a simple optical technique based on reflected light microscopy to perform microspectroscopy of a single NP placed in a conventional, nontransparent liquid delivery system. The insertion of a variable spot diaphragm in the optical path reduces the interference effect that occurs at the NP-substrate interface and improves the signal-to-noise ratio in NP imaging. Using this method, we demonstrated spatial imaging and spectral analyses of 60-, 80-, and 100-nm single gold NPs. A single-NP sensor based on a 100-nm NP was used for real-time measurement of bulk refractive index changes in the microfluidic channel and for detection of fast dynamic poly(ethylene glycol) attachment to the NP surface. Finally, electrochemical single-particle microspectroscopy was demonstrated by using a methylene blue electroactive redox tag. The proposed optical approach is expected to significantly improve the miniaturization and multiplexing capabilities of high-throughput biosensing based on single NP. © *2015 Society of Photo-Optical Instrumentation Engineers (SPIE)* [DOI: 10.1117/1.JBO.20.9.097001]

1 Introduction

Single plasmonic nanoparticle (NP) sensors have introduced a completely new dimension to the sensing scale and opened the way to an experimental realization of massive multiplexing and high throughput in diagnostics and drug discovery.[1,2] Plasmonic NP is in many ways the smallest biophysical transducer, giving unprecedented access to biochemical events at the molecular level. A NP's resonance excitation of localized plasmonic oscillation is sensitive to the NP's environment, charge, and size and is detected in the far field by optical microspectroscopy in the form of NP scattering,[3–7] absorption,[8,9] or extinction.[10] Successful implementation of single-particle biosensing technology equally depends on the performance and simplicity of the NP imaging setup and adapted fluidic system. To fully realize single-particle biosensing, a potential fluidic system has to satisfy at least the following requirements: easy integration into optical setup, simple replacement of biosensing chip, low cost for disposable tests, capacity to maintain optimal conditions for the functioning of biological objects (living cell incubator), ability to deliver a microvolume of analyte to the sensing area via fluidic microchannels, and capacity for complimentary biosensing technique application (electrochemistry). Single-particle plasmon spectroscopy usually employs dark-field microscopy (DFM) in transmission mode. However, the transmission microscopy can only operate with transparent microfluidic chambers. Furthermore, the available distance between the dark-field condenser and imaging objective in DFM imposes a very strict thickness limitation on the microfluidic setup,

especially when used with oil immersion. Such limitations complicate single-NP sensor development and significantly reduce the area of its application.

In this article, we propose using reflected light microscopy (RLM) for single plasmonic NP imaging and optical microspectroscopy. We recently demonstrated this technique applied to the spatial localization and spectral identification of plasmonic NPs with different compositions (gold, silver, and alloys) in a cellular environment.[11] It was shown that 60-nm NPs were reliably detected and spectrally identified over the background of light diffused by living cells. However, visualization and spectral identification of a single plasmonic NP attached to the substrate is greatly influenced by interference between the background reflection and the NP scattered field.[12] In the article, we demonstrated that introducing a diaphragm spot into the RLM optical setup allows us to acquire the correct NP spectrum with a signal-to-noise ratio (SNR) higher than that of DFM. For single-particle biosensing, such a modified RLM could provide efficient solutions to satisfy the above-mentioned requirements for an integrated liquid delivery system. We experimentally demonstrated that this optical approach can be easily combined with the conventional microfluidic systems found in different biosensing devices that are typically fabricated with teflon, plastic, or other chemically resistive and, most importantly, opaque materials. Because the illumination and detection spots are formed by the same optics and confined to the surface, the detection of a single NP in micrometric-sized microfluidic channels fabricated, for example, in a silicon wafer is also possible and really simple. Single-NP biosensing using electrochemical transducers offers a very attractive approach to converting the

*Address all correspondence to: Sergiy Patskovsky, E-mail: spatskovsky@polymtl.ca

results of biochemical events into a measurable analytical signal.[13,14] A good example of an electroactive redox tag is methylene blue (MB), which changes its absorbing oxidized state to colorless leucomethylene blue under a reduction potential of approximately −0.27 volts. Spectroelectrochemical analysis of the optical transmission variation generated by the electrochemical oxidation−reduction of MB has been experimentally realized by using an optical waveguide platform[15,16] and the electrochemical surface plasmon resonance (eSPR) biosensing technique.[17,18] In this article, we demonstrated electrochemical modulation of the optical spectrum for a single plasmonic NP submerged in an MB electroactive redox tag solution. In this case, an open cell with a conventional large reference and counter electrode was used for three-electrode potentiometric scanning.

2 Experimental Section

2.1 Chemicals and Materials

Accurate spherical gold NPs with sizes of 60, 80, and 100 nm in DI water were purchased from Nanopartz Inc., and 5-kDa Thiol PEG (mPEG-SH) was purchased from Nanocs Inc. (Boston, Massachusetts). MB and all other reagents were obtained from Sigma Aldrich (Oakville, Ontario, Canada).

Prior to gold NP immobilization, the glass coverslips were cleaned in a fresh "piranha" solution (H_2SO_4 3 : 1 H_2O_2), rinsed abundantly in DI water, and dried under a N_2 flow. A 10-μL drop of NP colloidal solution was placed on the substrate surface and gently dried with a N_2 flow.[5] Once dry, the sample was washed again in water to remove contaminants. Experiments confirmed stable NP attachments to the substrate surface during liquid flow in the microfluidic chamber.

2.2 Apparatus and Measurement

The RLM system for wide-field imaging and spectral examination of single plasmonic NPs was built on an inverted Eclipse Ti microscope (Nikon, Mississauga, Ontario, Canada) equipped with a 100× oil immersion objective (variable numerical aperture NA = 0.5 to 1.3). The output microscope image of the single plasmonic NP, which appears as an isolated bright dot, was either recorded by using a monochromatic camera (QIClick, QImaging, Surrey, British Columbia, Canada) or aligned with the input slit on an imaging spectrograph (Shamrock 550, Andor Technology, Belfast) equipped with a charge-coupled device detecting camera (Newton 940, 2048×512 pixels, Andor Technology) and a 150 lines/mm grating providing 364-nm bandwidths (Fig. 1). A flat-top inverted microscope motorized stage (ProScan, Prior Scientific Inc., Rockland, Massachusetts) allowed for fine three-dimensional (3-D) spatial sample translation and was used for single-NP alignment. In this optical configuration, a standard white light source (Nikon) with a 50-W halogen lamp provided a smooth illumination spectrum in an operating range from 400 to 764 nm. Custom-written LabView software controlled the motorized stage and performed real-time NP spectral acquisition and analysis. We have studied and experimentally tested several algorithms to find the spectral position of the resonance maximum, e.g., nine-order polynomial fits,[19] weighted centroid,[20] and dynamic tracking centroid algorithms.[21,22] In spite of its overall simplicity, the weighted centroid method demonstrated the best performance and was used to monitor real-time peak position. For comparison, conventional DFM in the transmission mode was used (dark-field condenser
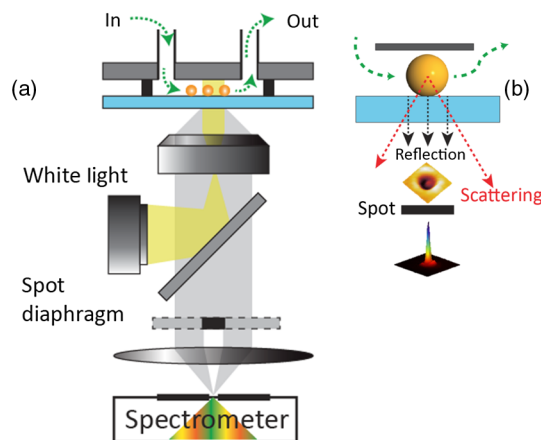

Fig. 1 (a) Reflected light microscopy setup using an imaging spectrometer. (b) The interference effect on the NP-substrate interface.

from Nikon, NA = 0.95 to 0.80). Experimental tests were performed with or without an additional blocking spot diaphragm (Fig. 1), the influence of which on the obtained results is discussed in the article.

The electrochemical experiments were controlled by a ModuLab potentiostat (AMETEK, Inc., Berwyn, Pennsylvania) in a three-electrode configuration. A single NP was deposited on a microscopy coverslip coated with a thin conductive indium tin oxide (ITO) layer, which serves as a working electrode. We used a 1-cm platinum disk as a counter electrode and an Ag/AgCl electrode filled with 3 M KCl electrolyte as a reference. The reference electrode was positioned 2 mm from the working electrode. Upon application of a voltage scan to the gold NP-ITO film, the NP spectral backscattering was analyzed providing an electrochemical biosensing response.

2.3 Fabrication of Microfluidic Systems

Several fluidic systems designed for particular applications were experimentally tested in this work. The first microfluidic system was fabricated from a 25-mm-diameter and 6-mm-thick polycarbonate material (Proto Labs, Inc., Maple Plain, Minnesota) [Fig. 2(c)]. Two 12-mm-long stainless steel tubes were inserted into 0.6-mm openings drilled into the polycarbonate, allowing simple attachments to the liquid delivery tubing. The microfluidic channel was shaped by a special O-ring cut from a 0.125-mm thick, double-sided SecureSeal adhesive sheet (Grace Bio-Labs, Oregon) using a femtosecond laser micromachining system that allowed us to fabricate microchannels with 5-μm precision. In our case, we tested a 6 mm $\times$ 500 μm $\times$ 125 μm single channel. The clean or NP-functionalized microscope coverslip was then attached to the microfluidics, and the whole system was affixed within the inversed microscope using a cage plate holder for Ø1-type optics (Thorlabs, Newton, New Jersey). A second microfluidic system provided a 1 mm $\times$ 50 μm $\times$ 50 μm channel fabricated into silicon by deep reactive ion etching [Fig. 2(b)]. It allowed us to test the RLM approach for the visualization and microspectroscopy of NPs placed into a microchannel made from nontransparent material. The potentiostatic three-electrode electrochemical tests were performed in the open cell fluidic system [Fig. 2(c)]. It was built on petri dishes with glass bottoms that were coated with an ITO layer (SPI Supplies, West Chester, Pennsylvania). Spring-loaded electrodes (Interconnect Devices, Kansas City, Kansas) were wired to
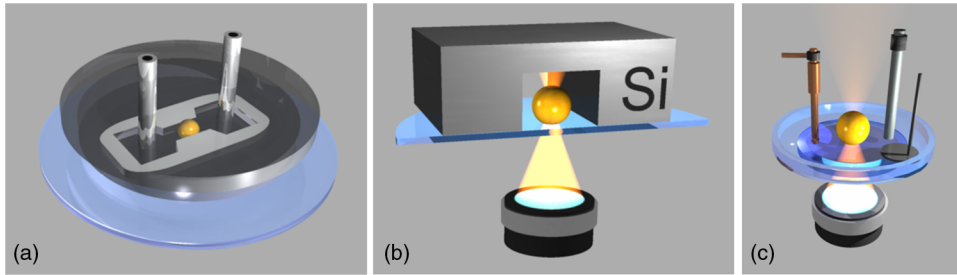
Fig. 2 Fluidic systems for single-NP biosensing. (a) Fabricated from bulk plastic materials. (b) Fabricated from silicon by deep reactive ion etching. (c) Open cell for single-NP electrochemical tests.

the potentiostat and provided contacts to the ITO layer directly through the liquid medium. During measurements, the whole setup was placed on an inverted microscopy stage. A syringe pump (Cole-Parmer, Montreal, Québec, Canada) was used to deliver liquid to the sensing particle placed into microfluidics in a smooth and continuous way, eliminating liquid pulsing inherent to the peristaltic pumps.

3 Results and Discussion

An RLM setup (Fig. 1, without spot diaphragm) was used to image a single 100-nm-diameter spherical gold NP deposited on a glass substrate and placed into a microfluidic system filled with DI water. As opposed to DFM, there is no limitation on the NA of the imaging objective in our setup; therefore, we initially used the maximum available 1.3 aperture. We obtained a bright spot image of the gold NP with an SNR of 10.8, as shown in Fig. 3. On the same figure, we compare the intensity profiles measured using five different NAs (0.5, 0.7, 0.8, 1.1 and 1.3) with a variable-aperture 100× oil immersion objective. It is obvious that the NP contrast is proportional to the NA, except for the lower 0.5 NA. In this case, the detected intensity profile
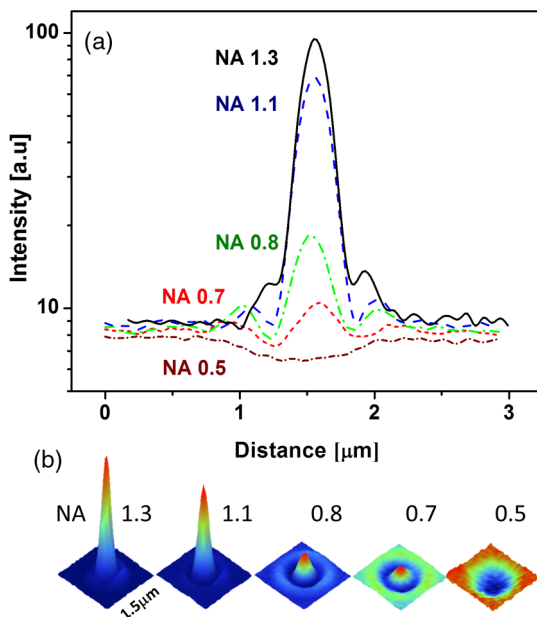
passed from positive to negative [Fig. 3(a)], and consequently, a dark spot was detected on the image [Fig. 3(b)].

Essentially, in our experiments, we measure interferometric intensity $Im = |E_{ref} + E_{sca}|^2$ that originates from the reflected field of the incident beam $E_{ref} = rE_{inc}$ and the scattered field by the single NP $E_{sca} = sE_{inc}$.[23] Here, E_{inc} is the field of the illumination light, r is the reflectivity of the glass–water medium interface, and $s(\lambda) = \eta D\alpha(\lambda)$, where $\alpha(\lambda)$ is the wavelength-dependent polarizability of the NP, η is a proportionality factor describing the detection efficiency of the optical setup, and D is the diameter of the spherical NP.[12] The backscattering spectrum is then calculated by the intensity difference between the signal I_m for a single NP and the reference intensity $I_{ref} = |E_{ref}|$,[2] measured away from the NP and normalized by the reference intensity:

$$\sigma_{sca}(\lambda) = \frac{I_m(\lambda) - I_{ref}(\lambda)}{I_{ref}(\lambda)} = \frac{\eta^2}{r^2}|\alpha(\lambda)|^2 - 2\frac{\eta}{r}|\alpha(\lambda)|\sin\varphi(\lambda).$$

(1)

The first term in Eq. (1) corresponds to pure scattering and drops for a spherical NP with the diameter D.[6] The second term in Eq. (1) scales as D^3 and therefore does not drop as fast. It dominates for smaller particles, and their resonance profiles become purely absorptive, which produces a dark spot on the image. A related interferometric detection scheme was experimentally realized for optical detection of very small 5-nm gold NPs on the surface[9] and for fast tracking of 25-nm Au particles in liquid.[24] In our case, similar transformation is obtained by controlling the detection efficiency of the optical setup η using an objective with a variable NA. Microspectroscopy results for the 100-nm Au NPs deposited on the glass substrate using an objective with varying NA are presented in Fig. 4. As predicted by the theory, for smaller NA, the resonance peak position shifts to a shorter wavelength, and for 0.5 NA, the NP spectrum shows an absorptive profile. As can be concluded from Figs. 3 and 4, the 100-nm gold NP intensity profile and spectrum detected with the 1.3 NA objective are dominated by scattering; thus, RLM can still be recommended as a method for single-NP biosensing for rather large NPs. However, the method fails for the smaller 60-nm NPs, where the intensity profile is caused by pure absorption, as shown in Fig. 4(b).

To tackle this problem, we propose a modified RLM technique that eliminates the NP interference effect in far-field imaging. In the optical setup, we introduced a central spot diaphragm (Fig. 1) after the beam splitter to block the light directly reflected from the substrate-medium interface. Such circular beam stops have already been applied in the optical path of the imaging objective to build objective-type vertical

Fig. 3 Experimental results obtained at five different NAs with an adjustable NA 100× oil immersion objective: 0.5, 0.7, 0.8, 1.1, and 1.3 NA. (a) Intensity profiles and (b) three-dimensional (3-D) images of nanoparticle (NP) point-spread function.
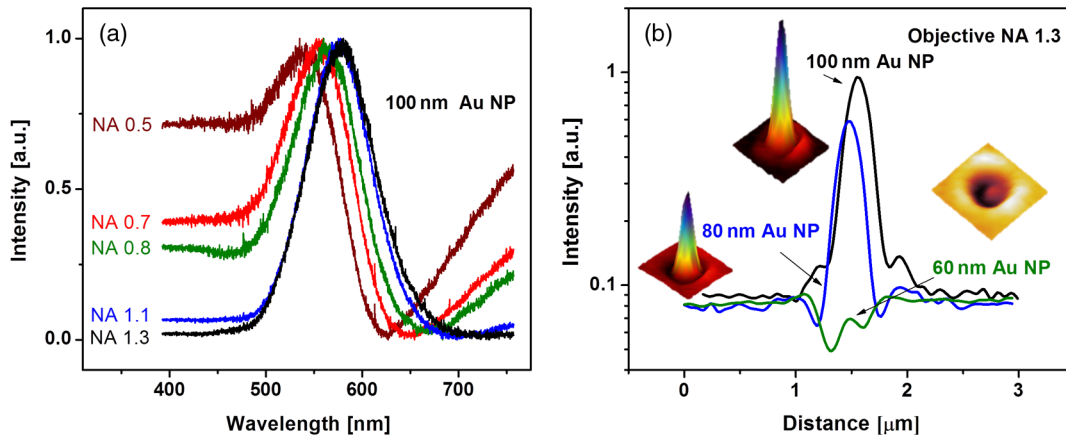
Fig. 4 (a) Experimental microspectroscopy results for the 100-nm Au NPs deposited on the glass substrate using an objective with a different NA and (b) 60-, 80-, and 100-nm-diameter NP intensity profiles.

illumination DFM[25] or to ensure effective suppression of the normally transmitted supercontinuum beam.[26] The diaphragm's function is to completely separate the illumination and scattering beam[27] because, in our case, we are only blocking part of the light normally reflected by the interface. It will also block the light backscattered from the NP, but only partially, because the NP can be considered as a point light source that scatters light in all directions and will be detected by an objective with high NA [Fig. 1(b)]. Only the central part of the image plane will be affected, which is acceptable for single-NP biosensing applications.

First, we verified this approach with 60-nm NPs deposited on the glass substrate and in a water medium. A 2-mm spot diaphragm was used, and the influence of the variable aperture on the experimental intensity profile is presented in Fig. 5(a). The resulting NP point-spread function keeps a conventional Gaussian shape up to the smallest NA of 0.5. The level of light rejection and affected field of view depend on the blocking spot size. A larger spot diameter could increase the working field of view on the image plane applied for NP detection [Fig. 5(a) (inset II)] and reduce the requirement for the collimating efficiency of the illumination beam. However, it also decreases the detected intensity and NP contrast, as shown in Fig. 5(a)

(Inset I). Therefore, with a coherent point source, a very small blocking spot can be realized.

Figure 5(b) shows some examples of experimental intensity distribution of the 60- and 100-nm NP point-spread functions for different optical approaches. The full width at half maximum of these functions was approximately 0.5 to 0.8 μm for the reflected light imaging mode (RLM) and at least three times larger, i.e., at 2 to 2.5 μm, in the dark-field mode (DFM). When we compare the SNR for 100-nm Au on the glass substrate, RLM with a 2-mm spot gives an SNR = 87, conventional RLM_SNR = 10.8 and DFM_SNR = 6.34. We can conclude that for the tested NP sizes (60, 80, and 100 nm), the proposed reflected light imaging mode with an additional spot diaphragm provides NP point-spread functions dominated by scattering, and due to the higher NA of the objective, offers better NP imaging contrast and can spatially localize the NPs with improved precision.[28]

Resonance-shift-based single-NP biosensors rely on the continuous measurement and comparison of the resonance peak position, which usually serves as the main sensing parameter. We verified the influence of the 2-mm spot diaphragm on the shape and position of the experimental NP scattering spectrum measured with RLM. For comparison, conventional DFM
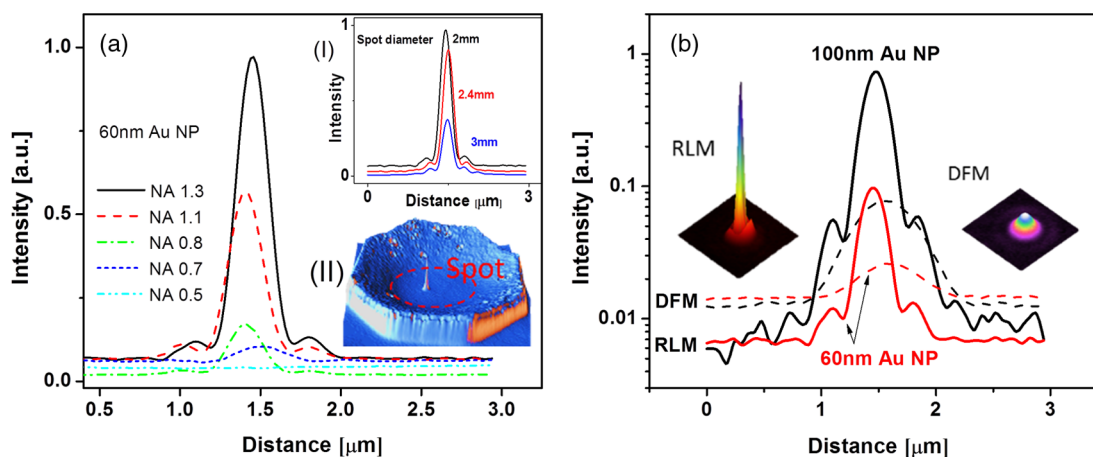

Fig. 5 (a) Experimental intensity profiles of 60-nm NPs taken at different NA and with a 2-mm spot diaphragm. (Inset I) Intensity dependence on the spot diaphragm diameter. (Inset II) Microscopy image of the NP backscattering in the center of the blocking spot. (b) Comparison of the two microscopy approaches—reflected light with a blocking spot (RLM) and dark-field (DFM)—for NP imaging.

provides us with the NP spectra in transmission mode. As shown in Fig. 6, the NP-substrate interference effect in RLM shifts the resonance peak position for larger 80- and 100-nm NPs and completely inverses the peak profile for smaller 60-nm NPs. However, we found very similar scattering spectra in the conventional DFM and with the reflected light method with the blocking spot. For example, the 100-nm Au NP resonance peak position was detected at 586.8 nm for DFM, 587.6 for RLM with the 2-mm spot and at 578 nm for RLM without a spot. Theoretical prediction using Mie theory gives similar scattering peak positions in a medium with a refractive index (RI) of 1.37 (586.6 nm), which is different from the 1.33 RI of our working solution (water). It is obvious that in the case of NP directly attached to the glass surface, an accurate theoretical estimation needs to take into consideration the substrate effect.[29] The resulting effective medium around NP (n_{eff}) will be included in the Mie calculation for theoretical evaluation.[30] In our case, the effective medium has $n_{eff} = 1.37$, which allows us to estimate an appropriate weighting factor α for the medium and substrate indices:

$$\alpha = \frac{n_{eff} - n_{substrate}}{n_{medium} - n_{substrate}}. \qquad (2)$$

With the BK7 glass substrate (1.51 RI) and water working medium (1.33 RI), we obtain a weighting factor $\alpha = 0.78$ that is in the range of values (0.7 to 0.82) presented in the literature.[30] As shown in Fig. 6, a similar weighting factor given an effective medium $n_{eff} = 1.37$ can be used for 60- and 80-nm NPs. The negative influence of the surface effect on the single-NP sensor sensitivity can be reduced by immobilizing NPs on either an SiO_2 intermediate layer[31] or a cytop or teflon cladding layer, which have an RI slightly above and slightly below, respectively, that of deionized water.[32] We can conclude from Fig. 6 that introducing a diaphragm spot into RLM and considering the substrate effect provides the correct positions of the resonance spectra for different NP sizes.

To test out RLM with a spot diaphragm, we performed real-time detection of medium bulk RI and thin biofilm formation on the surface of a single plasmonic NP in the microfluidic system previously described in the article. The backscattering spectrum of 100-nm gold NPs was detected by an imaging spectrometer and was treated by a home-made LabView-based program. The spectrum peak position and intensity were used as the two sensing parameters to monitor real-time changes in RI. As we already demonstrated in this article, using an immersion objective with high NA improves spatial 3-D localization compared to DFM. However, such an optical system is more vulnerable to the mechanical instability of the experimental setup. To minimize mechanical drift of the single-NP sample, we use an imaging spectrometer with a rather large slit size (100 μm) because spectral resolution is mostly defined by the focused spot size on the entrance slit. In the y-direction of the imaging detector, we combine five lines and automatically follow the central line with maximal intensity. In the z-direction, we manually readjust the focal position in our setup, whereas an autofocusing feature could greatly improve stability.

In Fig. 7(a), we present the result for bulk RI detection when deionized water in the microfluidic channel was replaced with a NaCl solution, effectively changing the medium RI from 1.33 to 1.38. The acquisition time constant for one point is 300 ms, and we then applied 6-point dynamic averaging for the final curve presented in the figure. We estimated the noise level and corresponding experimental resolution to be approximately 0.1 nm, with a bulk RI sensitivity of 95 nm/RI. The red line in Fig. 7(a) corresponds to the temporal response of the intensity of the resonance peak. With the intensity parameter, we observe an even more reliable and stable result, with an estimated resolution comparable to a 0.015-nm shift in the resonance peak position. In the inset of Fig. 7(a), we show theoretical scattering spectra using Mie theory for 100-nm gold NPs in the two different media, i.e., water and the NaCl solution. Considering the substrate effect on the effective medium RI [Eq. (2)], calculation was performed for 1.37 RI (Water) and 1.41 RI (NaCl solution). Experimental results demonstrated on average a 4.73-nm spectral shift, whereas the Mie theory predicts a 6.5-nm shift. The difference can be explained by the simplified calculation method using the weighting factor α for the substrate effect and the existence of residual contaminants still present on the NP surface.
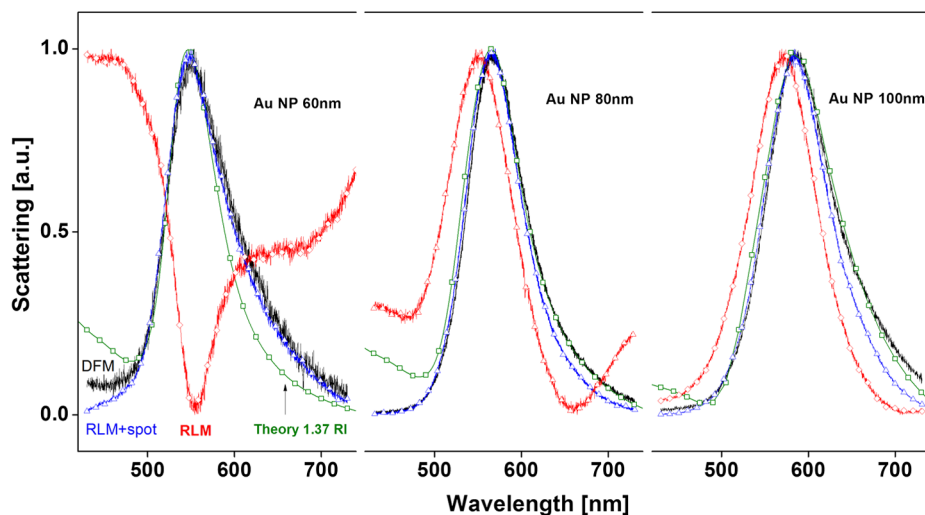

Fig. 6 Nanoparticle scattering spectra obtained with different optical techniques: dark-field microscopy (DFM, black), reflected light microscopy with a 2-mm spot (RLM+spot, blue), and reflected-light microscopy without a spot (RLM, red). The fitted theoretical peaks are shown in green for 60-, 80-, and 100-nm Au NPs.
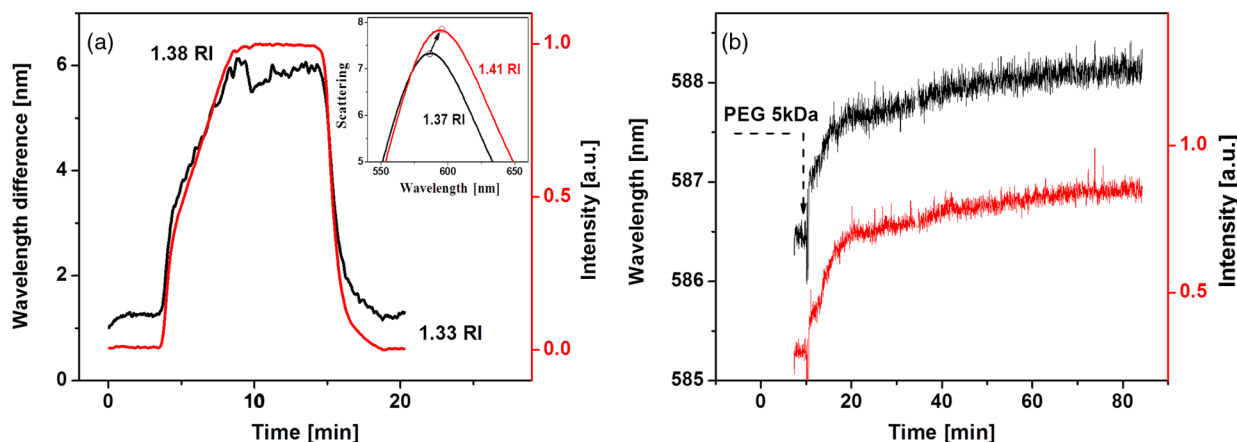
Fig. 7 (a) Single-NP sensor for bulk refractive index (RI) detection. (Inset) Theoretical spectra for 1.37 and 1.41 RI. (b) Real-time dynamics of nanoparticle surface functionalization with 5-kDa PEG-SH.

Single-NP biosensing usually implies real-time detection of biochemical reactions on the particle surface that leads to the formation of a thin biofilm with different RI. We verified our optical setup performance by measuring dynamics of NP surface functionalization with PEG. A thiol-ending polyethylene glycol (PEG-SH) compound performed well as a stabilization agent for gold NP colloidal stability[33] and has been applied as plasmonic markers in cellular recognition and analysis.[34] Verification of NP functionalization dynamic and efficiency on a single-particle level is important for the development of a reliable chemical protocol. For these experiments, we used a fluidic system with a $1~\text{mm} \times 50~\mu\text{m} \times 50~\mu\text{m}$ microchannel fabricated in a silicon wafer [Fig. 2(b)]. Initially, we verified the influence of the microchannel size on the NP imaging contrast. We observed that in planar directions, the limiting parameter is the excitation spot size, which could be as small as the optical system diffraction limit. As a result, RLM eliminates parasitic reflections from the microchannel walls, whereas the dark-field method requires special diaphragm geometry[35] and a transparent fluidic system. However, the depth of the microchannel becomes a limiting parameter for RLM NP imaging because a rather smooth silicon surface efficiently reflects light. We have found that in a microchannel with a depth equal to 30 μm, 100-nm NPs show an SNR that is approximately two times lower than for 100-μm microchannel depth. The results for the real-time dynamic of NP surface functionalization with 5-kDa mPEG-SH are shown in Fig. 7(b). As with bulk RI measurements, the resonance peak position and intensity show similar temporal trends after the injection of a 0.025 mg/mL mPEG solution. It is obvious that 80% of PEG attachments occur in the first 7 min and that the final layer stabilization takes approximately 1 h.

The RLM method proposed in this article allows for very simple experimental realization of electrochemical single-NP microspectroscopy [Fig. 2(c)]. Three-electrode potentiometric schema were used with conventional large size reference and counter electrodes. 100-nm gold NPs were deposited on a microscopy coverslip coated with a thin conductive ITO layer. In Fig. 8, we demonstrated gold NP spectrum peak voltammograms obtained with a 20 mv/s scanning rate in a 1-mM MB solution. Four consecutive scans showed similar and stable responses with a deviation point close to −0.27 V. We observed a NP spectrum shift to a higher RI value for MB in a reduced form. This is explained by the principle of absorption-based SPR,[36] where amplitude and direction of the SPR shift
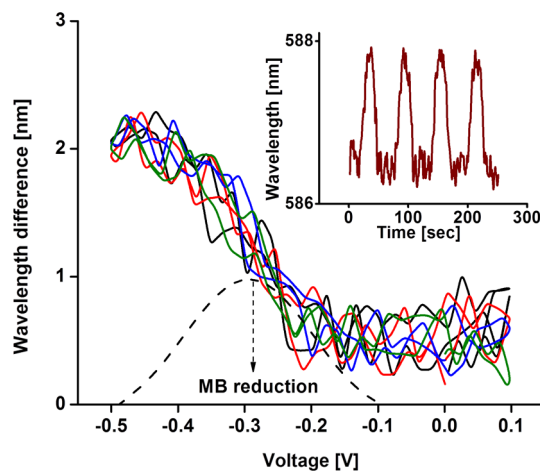

Fig. 8 100-nm gold NP spectral resonance peak position voltammograms obtained with a 20 mv/s scanning rate in a 1-mM MB solution. The four consecutive scans are shown using different colors. (Inset) Resonance peak position temporal response to 0.1 V(−0.5 V) voltage scan.

depending on the relative position of the MB resonance absorption at 664 nm and NP plasmonic resonance peak detection, which is performed at a lower wavelength of 587 nm. The obtained results confirm single-NP sensitivity to the variation of electrochemical local optical properties, and we believe that this nanoplasmonic eSPR technique is a promising technology for improving selectivity and sensitivity in localized and multiplexed biosensing.

4 Conclusion

Single-NP sensors can fully realize their biosensing potential if the optical setup allows for simple integration of different fluidic systems: flow through for continuous tests, injection type for disposable sensors, a fluidic chamber with micrometric-sized channels for extremely small volume samples, and a bulky open fluidic cell for electrochemical plasmonic sensing. Here, a reflected light optical mode presents a worthy and cost-effective alternative to DFM. In this article, we demonstrated its simple optical setup with a high NA objective, ease of NP illumination and localization, and ability to work with bulky

and nontransparent fluidics while delivering sufficient NP back-scattering intensity for real-time NP microspectroscopy.

Acknowledgments

References

1. J. N. Anker et al., "Biosensing with plasmonic nanosensors," *Nat. Mater.* **7**(6), 442–453 (2008).
2. T. Sannomiya and J. Voros, "Single plasmonic nanoparticles for biosensing," *Trends Biotechnol.* **29**(7), 343–351 (2011).
3. A. Wax et al., "Comparative review of interferometric detection of plasmonic nanoparticles," *Biomed. Opt. Express* **4**(10), 2166–2178 (2013).
4. J. R. G. Navarro and M. H. V. Werts, "Resonant light scattering spectroscopy of gold, silver and gold-silver alloy nanoparticles and optical detection in microfluidic channels," *Analyst* **138**(2), 583–592 (2013).
5. A. D. McFarland and R. P. Van Duyne, "Single silver nanoparticles as real-time optical sensors with zeptomole sensitivity," *Nano Lett.* **3**(8), 1057–1062 (2003).
6. I. Ament et al., "Single unlabeled protein detection on individual plasmonic nanoparticles," *Nano Lett.* **12**(2), 1092–1095 (2012).
7. V. Claudio, A. B. Dahlin, and T. J. Antosiewicz, "Single-particle plasmon sensing of discrete molecular events: binding position versus signal variations for different sensor geometries," *J. Phys. Chem. C* **118**(13), 6980–6988 (2014).
8. M. A. van Dijk et al., "Absorption and scattering microscopy of single metal nanoparticles," *Phys. Chem. Chem. Phys.* **8**(30), 3486–3495 (2006).
9. V. Jacobsen et al., "Interferometric optical detection and tracking of very small gold nanoparticles at a water-glass interface," *Opt. Express* **14**(1), 405–414 (2006).
10. L. S. Slaughter et al., "Single-particle spectroscopy of gold nanorods beyond the quasi-static limit: varying the width at constant aspect ratio," *J. Phys. Chem. C* **114**(11), 4934–4938 (2010).
11. S. Patskovsky et al., "Hyperspectral reflected light microscopy of plasmonic Au/Ag alloy nanoparticles incubated as multiplex chromatic biomarkers with cancer cells," *Analyst* **139**(20), 5247–5253 (2014).
12. K. Lindfors et al., "Detection and spectroscopy of gold nanoparticles using supercontinuum white light confocal microscopy," *Phys. Rev. Lett.* **93**(3), 037401 (2004).
13. Y. M. Fang et al., "Plasmonic imaging of electrochemical oxidation of single nanoparticles," *J. Am. Chem. Soc.* **136**(36), 12584–12587 (2014).
14. M. T. Castaneda, S. Alegret, and A. Merkoci, "Electrochemical sensing of DNA using gold nanoparticles," *Electroanal* **19**(7-8), 743–753 (2007).
15. B. M. Beam, N. R. Armstrong, and S. B. Mendes, "An electroactive fiber optic chip for spectroelectrochemical characterization of ultra-thin redox-active films," *Analyst* **134**(3), 454–459 (2009).
16. K. Imai et al., "Simultaneous multiselective spectroelectrochemical fiber-optic sensor: demonstration of the concept using methylene blue and ferrocyanide," *Anal. Chem.* **87**(4), 2375–2382 (2015).
17. Y. Iwasaki et al., "Analysis of electrochemical processes using surface plasmon resonance," *Sens. Actuators B* **50**(2), 145–148 (1998).
18. A. M. Dallaire et al., "Electrochemical plasmonic sensing system for highly selective multiplexed detection of biomolecules based on redox nanoswitches," *Biosens. Bioelectron.* **71**, 75–81 (2015).
19. P. P. Jia et al., "Plasmonic nanohole array sensors fabricated by template transfer with improved optical performance," *Nanotechnology* **24**(19), 195501 (2013).
20. K. Johansen et al., "Surface plasmon resonance: instrumental resolution using photo diode arrays," *Meas. Sci. Technol.* **11**(11), 1630–1638 (2000).
21. G. G. Nenninger, M. Piliarik, and J. Homola, "Data analysis for optical sensors based on spectroscopy of surface plasmons," *Meas. Sci. Technol.* **13**(12), 2038–2046 (2002).
22. A. B. Dahlin, J. O. Tegenfeldt, and F. Hook, "Improving the instrumental resolution of sensors based on localized surface plasmon resonance," *Anal. Chem.* **78**(13), 4416–4423 (2006).
23. J. Hwang and W. E. Moerner, "Interferometry of a single nanoparticle using the Gouy phase of a focused laser beam," *Opt. Commun.* **280**(2), 487–491 (2007).
24. B. Deutsch, R. Beams, and L. Novotny, "Nanoparticle detection using dual-phase interferometry," *Appl. Opt.* **49**(26), 4921–4925 (2010).
25. H. Ueno et al., "Simple dark-field microscopy with nanometer spatial precision and microsecond temporal resolution," *Biophys. J.* **98**(9), 2014–2023 (2010).
26. A. Weigel, A. Sebesta, and P. Kukura, "Dark field microspectroscopy with single molecule fluorescence sensitivity," *ACS Photonics* **1**(9), 848–856 (2014).
27. I. Braslavsky et al., "Objective-type dark-field illumination for scattering from microbeads," *Appl. Opt.* **40**(31), 5650–5657 (2001).
28. R. J. Ober, S. Ram, and E. S. Ward, "Localization accuracy in single-molecule microscopy," *Biophys. J.* **86**(2), 1185–1200 (2004).
29. M. D. Malinsky et al., "Nanosphere lithography: effect of substrate on the localized surface plasmon resonance spectrum of silver nanoparticles," *J. Phys. Chem. B* **105**(12), 2343–2350 (2001).
30. A. Curry et al., "Substrate effect on refractive index dependence of plasmon resonance for individual silver nanoparticles observed using dark-field micro-spectroscopy," *Opt. Express* **13**(7), 2668–2677 (2005).
31. A. Dmitriev et al., "Enhanced nanoplasmonic optical sensors with reduced substrate effect," *Nano Lett.* **8**(11), 3893–3898 (2008).
32. P. Berini, "Long-range surface plasmon polaritons," *Adv. Opt. Photonics* **1**(3), 484–588 (2009).
33. J. Gao et al., "Colloidal stability of gold nanoparticles modified with thiol compounds: bioconjugation and application in cancer cell imaging," *Langmuir* **28**(9), 4464–4471 (2012).
34. S. Patskovsky, E. Bergeron, and M. Meunier, "Hyperspectral darkfield microscopy of PEGylated gold nanoparticles targeting CD44-expressing cancer cells," *J. Biophotonics* **8**(1-2), 162–167 (2015).
35. C. Lin et al., *Objective-Type Dark-Field Illumination Device for Microfluidic Channel*, U.S. Patent No. 8625195 (2014).
36. K. Kurihara and K. Suzuki, "Theoretical understanding of an absorption-based surface plasmon resonance sensor based on Kretchmann's theory," *Anal. Chem.* **74**(3), 696–701 (2002).

Sergiy Patskovsky received his BS degree in Radiophysics Faculty from Taras Shevchenko University of Kiev in 1986 and his PhD from Polytechnique Montréal in 2005, where he is currently a research associate in the Engineering Physics Department. His research mainly focuses on plasmonic biosensing, biophotonics, and hyperspectral optical imaging.

Michel Meunier received his BIng and MScA degrees in engineering physics from Polytechnique Montréal in 1978 and 1980, respectively, and his PhD from the Massachusetts Institute of Technology in 1984. He is currently the director of the Laser Processing and Plasmonics Laboratory at Polytechnique Montréal. For 33 years, he has been involved in laser processing of various materials and biological applications, and he has published over 330 papers in this field.